



Investigation of the mechanical interaction of the trabecular core with an external shell using rapid prototype and finite element models

Title	Investigation of the mechanical interaction of the trabecular core with an external shell using rapid prototype and finite element models
Author(s)	Mc Donnell, Patricia E.; Harrison, Noel M.; Lohfeld, Stefan; Kennedy, Oran; Zhang, Y.; McHugh, Peter E.
Publication Date	2009-04-05
Publisher	Elsevier
Repository DOI	10.1016/j.jmbbm.2009.03.002



Investigation of the mechanical interaction of the trabecular core with an external shell using rapid prototype and finite element models

P.Mc Donnell^{a,b}, N.Harrison^{a,b}, S.Lohfeld^{a,b}, O.Kennedy^c, Y.Zhang^{a,b}, P.E.Mc Hugh^{a,b}

^a National Centre for Biomedical Engineering Science, National University of Ireland, Galway, Ireland

^b Department of Mechanical and Biomedical Engineering, National University of Ireland, Galway, Ireland

^c Trinity Centre for Bio-Engineering, Trinity College Dublin, Ireland

Abstract

The mechanical properties of vertebral bone have been widely studied with the ultimate goal of improving fracture risk prediction. However, the mechanical interaction between the cortical shell and the trabecular core is not well understood. The objective of this study was to investigate this interaction and to determine what effect it has on the ultimate strength of the whole bone. This objective was achieved by compression testing rapid prototype (RP) models of cylindrical trabecular bone cores, with and without an integral surrounding shell and incorporating increasing levels of artificially induced bone loss. Corresponding finite element (FE) models were generated and the load sharing of the shell and trabecular core was analysed under linear elastic loading conditions. The results of the physical RP model tests and corresponding FE analyses indicated that there was a reinforcing effect between the cortical shell and the trabecular core for all models tested and that the reinforcing effect became relatively more important to the ultimate strength of the whole bone as the bone volume fraction of the trabecular core decreased. It was found that two mechanisms contributed to the reinforcing effect: (i) load transfer from the highly stressed shell into the connecting outer trabeculae of the core for the shelled model. This did not occur for the un-shelled model where the load dropped off at the outer unsupported trabeculae; (ii) the stiffening effect on the shell due to the support provided by the connecting struts of the trabecular core, which serves to inhibit bending and buckling behaviour in the shell under compression loading. It was found that the stiffening on the shell was the more dominant contributor to the overall reinforcing effect between the shell and the trabecular core.

1. Introduction

The mechanisms by which bone strength and stiffness deteriorate as bone loss progresses with aging have been extensively studied and many of these studies have focussed on trabecular bone properties (Ding et al., 2002, Homminga et al., 2001, Mosekilde, 1990, Muller and Ruegsegger, 1996, Silva and Gibson, 1997, Tanck et al., 2006, Thomsen et al., 2002b, van der Linden et al., 2002). Trabecular bone strength has typically been quantified experimentally by performing compression tests on cylindrical specimens which have been cored out from the whole bone (Bayraktar and Keaveny, 2004, Homminga et al., 2002, Keaveny, 1993, Keaveny, 1997, Linde, 1989). Although such experiments have yielded valuable information on the strength and modulus properties of trabecular bone, the important contribution of the cortical

shell to the overall bone strength is not taken into account, thus limiting the application of such data for predicting whole bone fracture loads. In particular, the mechanical interaction between the cortical shell and the trabecular core in vertebrae is not well understood, although recent finite element studies on whole vertebrae suggest that this may have an important contribution to the whole bone strength and stiffness (Bayraktar et al., 2003, Eswaran et al., 2007b).

The current study was performed to investigate the mechanical interaction between the shell and trabecular core for vertebral bone using a novel combination of rapid prototype (RP) model testing and finite element (FE) modelling. Specifically, it was desired to determine the effect of this interaction on the ultimate strength of the shell–core structure by compression testing rapid prototype (RP) models of ovine vertebral trabecular bone. FE modelling of the trabecular core structures could then be used to perform a decoupling analysis on this interaction effect, in order to determine the relative importance of the reinforcement of the shell due to its mechanical interaction with the trabecular core (shell reinforcing effect), versus the reinforcement of the trabecular core due to its mechanical interaction with the connecting shell (core reinforcing effect).

RP models are three-dimensional physical biomodels (Lohfeld et al., 2005) which are derived from micro-computed tomography (μ CT) scans of the bone samples (Fig. 1). The Selective Laser Sintering (SLS) process was used in this study, in which a laser sinters the profile, slice by slice in a powder bed, until the completed 3D structure is produced. Previous studies on RP models of trabecular bone have compared their mechanical behaviour with micro-FE models (Dobson et al., 2006, Su et al., 2007, Zysset et al., 1997), and preliminary comparison studies have been made with real bone (Umeno et al., 2006). However, it has not yet been determined if RP models exhibit realistic strength and failure characteristics compared to real bone. Therefore, an initial study was performed as part of this work to justify the use of RP models by comparing the ultimate strength and visual failure mechanisms of RP models with those of corresponding real bone specimens. Ovine trabecular bone specimens were used since previous studies have shown that this provides an appropriate large animal model for analysis of the mechanical behaviour of bone (Newton et al., 2004, Pouilles et al., 2000, Thomas et al., 1996).

Pending the successful outcome of this verification study, our specific objectives were: (i) to quantify the extent of the reinforcing effect between the shell and the trabecular core on the ultimate strength of the whole structure; (ii) to evaluate if this reinforcing effect becomes more important to the whole bone strength as the trabecular core bone volume fraction decreases; (iii) to determine the relative importance of the shell reinforcing effect compared to the core reinforcing effect.

2. Materials and methods

2.1. Comparison of RP models with real bone specimens

Compression tests were performed on RP models of ovine vertebral trabecular bone and corresponding real bone specimens to determine if RP models were suitable for subsequently comparing the strength characteristics of trabecular architectures with increasing levels of bone loss. Twenty cylindrical trabecular specimens were extracted from ovine L5 lumbar vertebrae. The mean and standard deviation of the bone volume fraction (BV/TV) for the trabecular specimens was 0.33 ± 0.04 (range of 0.25–0.43). A diamond impregnated coring tool was used to extract the specimens and a clamping fixture ensured that they were aligned in the inferior-superior direction of the vertebra. The 7 mm diameter specimens were converted to square

cross-section using a slow speed diamond saw (Buehler, Isomet). This specimen shape facilitated viewing under the microscope in the subsequent compression tests. The finished specimens had dimensions of 4.5 mm by 4.5 mm by 25 mm length. The specimens were water-jet cleaned to remove marrow and coring debris. Specimens were kept hydrated at all times and stored in sealed plastic bags at $-18\text{ }^{\circ}\text{C}$ prior to testing.

The specimens were μCT scanned at $6\text{ }\mu\text{m}$ resolution (μCT 40, SCANCO Medical AG, Switzerland). The image slices were coarsened to $24\text{ }\mu\text{m}$ resolution and were converted into 3D STL reconstructions (Mimics 9.0, Materialise RapidParts, UK). Each STL file was imported into the build setup software for the RP laser sinterstation (SLS 2500 Plus, DTM Corporation, USA). The maximum resolution of the sinterstation is 0.1 mm. Therefore, the models were scaled up by 10 times so that trabecular features with a size scale of the order of 0.01 mm in the real bone specimens could be captured in the corresponding RP replica (Fig. 1). Duraform PA-12 powder was the raw material used (3D Systems, UK). The energy density of the sintering laser was set to 0.016 J/mm^2 . Prior process parameter studies at our laboratory have shown that this level of energy density results in modulus and strength properties which are very similar in the vertical and transverse directions of the RP build (Caulfield et al., 2007).

The real bone specimens were mounted in brass end-caps to reduce end artifacts during compression testing (Keaveny, 1997, Kopperdahl and Keaveny, 1998). The depth of specimen in each end-cap was 7 mm, resulting in a central free length of approximately 10 mm. Specimens were tested in compression using a 1 kN load capacity testing machine (Zwick model BZ2.5, UK). A microscope and digital camera allowed a clear image to be obtained of one face of the specimen at 20X magnification. Video capture software recorded a video of the test directly to a PC. The test speed was 0.1% strain per second. Four pre-cycles to 0.5% strain were performed on each specimen and the specimens were loaded to failure on the 5th cycle.

The RP models were tested using an equivalent protocol on a 25 kN testing machine (Model 8874, Instron UK Ltd.) due to the higher loads required to destruct the 10X scaled-up models. A digital camera recorded a video of the test. Each model was tested to failure, or alternatively to the maximum 25 kN load capacity of the test machine, if failure did not occur.

A correction factor was determined to account for the difference in strength between the bone tissue material and the PA-12 material which was used to manufacture the RP models. Twenty bone tissue specimens were cut from the vertebral shells of the same vertebrae from which the trabecular cores were extracted (Fig. 2) using a slow speed diamond saw. Trabecular bone was carefully removed from the shell specimens using a scalpel, followed by polishing with a grit 320 P400 polishing disc (Metaserv 2000, Buehler UK Ltd.). The mean length, width and thickness of the specimens were 5.27 mm, 4.95 mm and 1.16 mm, respectively (Table 1). The specimens were inserted in an aluminium holder which provided support along the length of the specimens to a depth of 2.5 mm. They were secured using cyanoacrylate adhesive so that there was a free length of approximately 2.8 mm protruding from the holder, giving an aspect ratio (free length to thickness) of 2.4. The specimens were compressed in a testing machine (Model 8874, Instron UK Ltd) until failure occurred (Fig. 2) and the ultimate stress was calculated. Seven PA-12 specimens with similar dimensions (length 5.22 mm, width 4.46 mm and thickness 1.11 mm) were rapid prototyped, mounted in aluminium holders and tested to failure using the same protocol. The correction factor for the difference in strength between the real bone tissue and the PA-12 material was calculated as the ratio of the mean values of the ultimate strength obtained for each series of tests:

$$\text{Correction factor} = \frac{UTS_{bone}}{UTS_{PA-12}} \quad (1)$$

where UTS_{bone} and UTS_{PA-12} are the mean values of ultimate strength for bone tissue and PA-12 material, respectively.

The RP model ultimate strength results were compared with the corresponding real bone ultimate strength results on a specimen-by-specimen basis and also by determining the correlation coefficient between the RP and real bone results for the complete set of tests. In addition, the failure mechanisms and failure locations were analysed from the videos of the RP model tests and real bone tests to determine if the RP models failed in a qualitatively similar way to the real bone specimens.

2.2. Investigation of interaction between shell and trabecular core

The objective of this section of the study was to quantify the magnitude of the overall reinforcing effect on the ultimate strength due to the mechanical interaction between the shell and the trabecular core, for different values of trabecular core volume fraction. This objective was achieved by compression testing RP models of trabecular bone, with and without an integral shell. Cylindrical RP models with dimensions 48 mm diameter by 72 mm length (again scaled up by 10X magnification), were manufactured from the μ CT scans of 3 of the ovine trabecular core specimens. The cylindrical shape facilitated the application of an integral surrounding shell and was achieved by cropping the original μ CT scans using a custom MATLAB program (MATLAB version 6.5., The MathWorks, MA, USA) and subsequently generating a 3D STL reconstruction (Mimics 9.0, Materialise RapidParts, UK). The STL files were imported into a 3D surface modelling software package (DeskArtes Design Expert, Version 5.2.0., Helsinki, Finland) and the shells were applied by constructing a cylindrical surface primitive with the same length as the trabecular core. The internal diameter of the shell was 45 mm and the shell thickness was 1.5 mm. The shell was then positioned over the trabecular core so that the internal surface of the shell overlapped the outside surface of the trabecular core. The shell and core were then merged into a single STL entity.

A voxel mesh was created from the μ CT scans for each of the 3 ovine trabecular core specimens using a Fortran meshing program that had been previously developed by the authors (Harrison et al., 2008). An algorithm was developed to universally thin trabeculae and was incorporated into the meshing program. This surface erosion algorithm simulates secondary osteoporosis (e.g. during bed-rest or extended space travel) by uniformly removing voxel elements from the surface of the trabeculae (Guo and Kim, 2002, van der Linden et al., 2002). This process imposes trabecular thinning as well as perforation of trabeculae. A MATLAB program was developed to extract image slices from the thinned voxel models and 3D STL reconstructions were created from these image slices (Mimics 9.0, Materialise RapidParts, UK). RP models were then generated for 2 increasing levels of uniform bone loss, in addition to the original unthinned trabecular cores (Table 4). The RP builds included a model of the trabecular core (without a shell), the trabecular core with an integral shell and the shell on its own (Fig. 3). An additional trabecular core model was developed corresponding to a bone specimen with a diameter of 9.6 mm, with and without a shell. This model was used to investigate the effect of increasing the core size on the shell/core interaction. All RP models were tested to failure in compression using the procedure described previously (Fig. 4). The modulus values and ultimate loads were determined for the trabecular core, for the shell on its own and for the trabecular core with an integral shell.

The total load carried by the shell–core structure is broken down into the load carrying contributions of the trabecular core, the shell and the reinforcing effect between the core and the shell, as follows:

$$F_{SC} = F_C + F_S + F_R \quad (2)$$

where F_{SC} is the ultimate load carried by the shell–core structure, F_C is the ultimate load carried by the trabecular core, F_S is the ultimate load carried by the shell and F_R is the reinforcing load due to the shell/core interaction. The reinforcing load can then be calculated since the values of F_{SC} , F_C and F_S are determined from the experimental tests:

$$F_R = F_{SC} - F_C - F_S \quad (3)$$

2.3. Stiffness analysis and finite element modelling

Although the overall reinforcing load, F_R , between the shell and the core could be determined from the experimental tests on the RP models, it was desired to further decouple this reinforcing effect into the contributions of the shell reinforcing effect and the core reinforcing effect. A combination of FE analysis and experimental results were used to perform this decoupling analysis since it was not possible to determine the two separate reinforcing components from the experimental tests alone. The FE analyses were confined to the linear elastic region of the stress–strain curve, so that identification of the ultimate load point was not possible. Therefore, we focussed our decoupling analysis on the apparent modulus of the shell–core structure. However, since the strength of bone is highly correlated with its apparent modulus (Fyhrie and Vashishth, 2000, Goulet et al., 1994, Hou et al., 1998, Keaveny et al., 1994), this decoupling analysis could be used to infer the corresponding strength contributions of the shell reinforcing effect and the core reinforcing effect.

We can break down the modulus contributions to the overall stiffness of the shell–core structure in a fashion analogous to that given in Eq. (2), as follows:

$$E_{SC} = v_C E_C + v_S E_S + E_R \quad (4)$$

where E_{SC} is the apparent modulus of the shell–core structure, E_C is the apparent modulus of the trabecular core, E_S is the modulus of the shell, E_R is the overall contribution to modulus due to the shell/core interaction, v_C is the spatial volume fraction of the trabecular core and v_S is the spatial volume fraction of the shell. E_R can be decoupled into two components corresponding to the shell reinforcing effect and core reinforcing effect as follows:

$$E_R = v_C E_{RC} + v_S E_{RS} \quad (5)$$

where E_{RC} is the increased stiffness in the trabecular core due to its mechanical interaction with the shell (core reinforcing effect) and E_{RS} is the increased stiffness in the shell due to its mechanical interaction with the trabecular core (shell reinforcing effect). The values of the core reinforcing effect ($v_C E_{RC}$) and the shell reinforcing effect ($v_S E_{RS}$) can be obtained from a final breakdown of the shell–core apparent modulus which is achieved by substituting Eq. (5) into Eq. (4), as follows:

$$E_{SC} = v_C (E_C + E_{RC}) + v_S (E_S + E_{RS}) \quad (6)$$

The two unknown values in Eq. (6) are E_{RC} and E_{RS} , since E_{SC} , E_C and E_S are determined from the results of experimental tests, and the volume fractions, v_C and v_S , can be calculated from the spatial volumes of the shell and core. The value of E_{RC} can be determined by performing FE analyses on voxel models corresponding to the experimental specimens, in which the load carrying contributions of the shell and trabecular core regions are isolated into distinct radial annuli. By summing the load carrying contributions of the trabecular core annuli (i.e. excluding the shell annuli), the apparent modulus corresponding to just the trabecular core, E_{C1} , can be determined for the integrated shell–core structure. A corresponding model of the trabecular core without an integral shell yields an apparent modulus value of E_{C2} . The modulus contribution due to the core reinforcing effect, E_{RC} , can then be calculated as follows:

$$E_{RC} = E_{C1} - E_{C2}. \quad (7)$$

The modulus contribution due to the shell reinforcing effect, $v_S E_{RS}$, can now be determined by re-arranging Eq. (6), as follows:

$$v_S E_{RS} = E_{SC} - v_C (E_C + E_{RC}) - v_S E_S. \quad (8)$$

In order to determine the values of $v_C E_{RC}$, a separate FE voxel model was generated for each of the following cases: (a) un-thinned with integral shell; (b) un-thinned without a shell; (c) thinned with integral shell; (d) thinned without a shell. The voxel resolution was 48 μm for the 4.8 mm diameter specimens and 72 μm for the 9.6 mm diameter specimens. A linear elastic analysis was performed on each model using an element-by-element solver that had been developed previously by the authors (Harrison et al., 2008). A boundary condition of 0.5% compressive strain was applied to the nodes on the top surface of the cylindrical geometry and the nodes on the bottom surface were constrained in all degrees of freedom (Fig. 5). A tissue elastic modulus of 10 GPa and a Poisson's ratio of 0.3 were assigned to the model to represent bone tissue. A custom postprocessor code was written to divide each FE model into separate annuli (nominal radial thickness of 0.072 mm for the 9.6 mm models and 0.048 mm for the 4.8 mm models). The load carrying contribution of a particular annulus was calculated by multiplying the vertical stress component by the cross-sectional area for each voxel and summing for all voxels in the annulus. This procedure was performed for each voxel layer in the vertical direction and the average annulus load for all of the layers was calculated. The value of E_{RC} that was determined from these analyses (see Eq. (7)) was multiplied by a correction factor before substituting into Eq. (8), in order to account for the difference in modulus between the FE simulated bone tissue (10 GPa) and the PA-12 material that was used for the RP model experimental tests:

$$\text{Correction factor} = \frac{\text{Experimental apparent modulus of RP trabecular core}}{\text{FE apparent modulus of corresponding trabecular core}}.$$

3. Results

3.1. Comparison of RP models with real bone specimens

The mean values of the ultimate strength for the real bone tissue and the PA-12 material were found to be 104.30 ± 30.94 MPa ($n=20$) and 41.84 ± 3.25 MPa ($n=7$), respectively (Table 1). The correction factor for the difference in strength between the real bone tissue and the PA-12 material was subsequently calculated as follows:

$$\text{Correction factor} = \frac{UTS_{bone}}{UTS_{PA-12}} = \frac{104.30}{41.48} = 2.49.$$

The ultimate stress of the RP trabecular bone models was, as expected, less than that of the real bone specimens because the bone tissue material is stronger than the PA-12 material of the RP models. However, when the correction factor was applied, the strength results for the RP models were, on average, just 10.89% lower than the real bone specimens (Table 2). This is most likely due to the fact that the real bone tissue samples, which were used to determine the correction factor, contained small geometric imperfections which would increase the chances of buckling under compression loading, resulting in a lower correction factor than would be achieved for an ideal geometry. Good correlation was obtained between the individual specimen ultimate strength results for the RP replicas and the real bone specimens ($R^2 = 0.80$) (Fig. 6). Qualitative video examination of the compression tests showed similarities in deformation and failure mechanisms between the RP replicas and the corresponding real bone specimens (Fig. 7 and Table 3).

3.2. Investigation of mechanical interaction between shell and trabecular core

The ultimate strength values for the RP models with an integral shell were found to be greater than the sum of the strength contributions of the individually tested trabecular core and shell, for all models tested. This suggests that there is a reinforcing effect between the trabecular core and the shell which enhances the strength of the entire structure. The reinforcing effect was calculated as a percentage of the trabecular core strength for each model (Table 4). For the three un-thinned 48 mm diameter models (BV/TV range from 0.26 to 0.32), the percentage reinforcing effect varied from 22% to 24%. The percentage reinforcing effect increased for each specimen with increasing levels of artificially induced bone loss, suggesting that the reinforcing interaction between the trabecular core and surrounding shell has a greater influence on the overall strength as the trabecular bone volume fraction decreases.

The reinforcing effect of 2% for the 96 mm diameter, un-thinned model (BV/TV =0.45) was much lower than for the un-thinned 48 mm diameter models. This suggests that the reinforcing effect diminishes for high bone volume fraction specimens as the size scale approaches whole bone dimensions. For the corresponding thinned model (BV/TV =0.22), the reinforcing effect was found to be 60% of the isolated core strength (Table 4). The experimental stress–strain curves for the thinned 96 mm models (Fig. 8) show that the apparent modulus of the shelled model (101 MPa) is 2.73 times greater than the apparent modulus of the un-shelled trabecular core (37 MPa). For the un-thinned models, the difference in apparent modulus between the shelled and un-shelled models is much less (390 MPa for the shelled model, 330 MPa for the un-shelled model). The mean and standard deviation of effective modulus for the isolated shells was found to be 880 ± 70 MPa ($n = 5$) for the 48 mm diameter models, and 450 ± 31.5 MPa ($n = 5$) for the 96 mm diameter models.

3.3. Finite element modelling and stiffness analysis results

The FE analyses showed that the modulus of the trabecular core in the shelled models was consistently greater than the corresponding modulus in the un-shelled models, resulting in a trabecular core stiffness reinforcing effect $v_C E_{RC}$ (Table 5). An examination of the stress contour plots and annulus stress distributions reveals the mechanisms by which this stiffness reinforcing effect occurs (Fig. 9). High stresses occur in the shell region in the direction of the applied strain and are transferred into the trabecular core adjacent to the shell. This results in

higher average stresses for the outer annuli of the trabecular core compared to the corresponding model without a shell. For the thinned, 9.6 mm diameter model (BV/TV =0.22), the radial thickness of the annulus over which these higher stresses occur in the trabecular core is approximately 1.09 mm and is referred to as the trabecular core transition region. For the corresponding model without a shell, the average annulus stresses show a steady decrease towards the outer cylindrical surface for the same 1.09 mm outer annulus of the trabecular core. Beyond the trabecular core transition region (moving towards the centre of the cylindrical core), the stress distributions for the models with a shell and without a shell match almost exactly. The ratio of the stiffness reinforcing effect to the stiffness of the isolated trabecular core was calculated to be 10.44% for this model (Table 5). Similar trends in the annulus stress distribution were found for the un-thinned model (BV/TV =0.45). However, the size of the trabecular core transition region for this high volume fraction model is smaller (0.66 mm) and the stress differential between the shelled and un-shelled models is not as great, resulting in a much lower trabecular core stiffness reinforcing effect of 1.63% relative to the stiffness of the isolated trabecular core (Table 5).

The results of the decoupling stiffness analysis for the 48 mm and 96 mm diameter models (Table 5), show that the shell reinforcing effect is consistently greater than the corresponding core reinforcing effect. For example, the reinforcing effect that the trabecular core exerts on the shell for the 96 mm diameter thinned model (BV/TV =0.22) is 8.90 times greater than the reinforcing effect that the shell exerts across the trabecular core transition region. For the same model, the combined reinforcing effects of $v_C E_{RC}$ and $v_S E_{RS}$ contribute more than 38% of the total stiffness of the shell–core structure, E_{SC} .

4. Discussion

The morphological and mechanical properties of trabecular bone cores have been extensively studied, using both finite element modelling (Eswaran et al., 2007a, Follet et al., 2007, Harrison et al., 2008, Homminga et al., 2003, Homminga et al., 2001, Keaveny et al., 1994, Liebschner et al., 2005, Muller and Ruegsegger, 1995, Nazarian et al., 2006, Niebur et al., 2000, Verhulst et al., 2008, Yeni and Fyhrie, 2001) and experimental testing techniques (Arthur Moore and Gibson, 2002, Hulme et al., 2007, Keaveny, 1997, Nagaraja et al., 2005, Ohman et al., 2007, Perilli et al., 2008, Sran et al., 2007, Thomsen et al., 2002a), with the ultimate goal of improving fracture risk prediction. However, for vertebral bone it is widely acknowledged that the cortical shell also provides an important contribution to the load bearing ability of the whole bone (Andresen et al., 1998, Ito et al., 2002) and finite element studies have indicated that there is a mechanical interaction between the shell and the trabecular core which enhances the overall strength and stiffness properties of the whole vertebra (Bayraktar et al., 2003, Eswaran et al., 2007b). In this study, the novel approach of physically testing RP models of shelled and un-shelled trabecular bone cores, supplemented by FE analysis of corresponding voxel models, allowed us to investigate this mechanical interaction. A major benefit of this approach was the fact that it was not necessary to take into account the variables of tissue heterogeneity (Goldstein, 1987, Morgan et al., 2003) and microdamage (Wang and Niebur, 2006, Yeh and Keaveny, 2001) which occur in real bone, thus allowing the effects of architecture changes to be isolated.

A detailed validation study was initially performed to determine if RP models could provide a reasonable representation of the failure behaviour of trabecular bone. The results of this study indicated good correlation ($R^2 = 0.80$) between the ultimate strength results for individual real bone specimens and corresponding RP models (Fig. 6). Also, when an experimentally

determined correction factor was applied to the RP model results to account for the difference between the strength of real bone tissue and PA-12 material, the average difference between real bone strength and RP model strength was found to be just 10.89% (Table 2). It should be noted that the bone tissue strength results (104 MPa), which were used to determine this correction factor, are on the lower end of ultimate strength values reported in the literature for cortical bone (100–200 MPa) (Liebschner, 2004). This may be due to fact that only relatively thin cortical specimens could be extracted from the vertebral shell (average thickness of 1.16 mm) and these specimens incorporated slight curvatures due to the vertebral geometry. This non-standard specimen geometry would be more prone to buckling under compression loading compared to the larger specimens which are normally used to determine the compression strength of trabecular bone. However, since the PA-12 specimens also had the same average dimensions as the vertebral tissue specimens, it is considered that the correction factor determined from this comparison provides a reasonable estimate of the difference in strength between the bone tissue and the PA-12 material.

Further support for the use of RP models was provided by the video examination of the failure mechanisms of the real bone specimens and corresponding RP models. This showed that the failure locations and mechanisms were qualitatively similar for many of the specimens (Table 3 and Fig. 7). These combined results supported the conclusion that RP models could be used as a surrogate for real bone when evaluating trends in ultimate strength properties due to changes in the architecture of the bone. A caveat to this conclusion is the critical requirement to closely control the preparation of the RP building material and the RP processing parameters in order to minimise variations in the material properties of the models that are built.

RP models were subsequently manufactured from μ CT scans of 4 different ovine L5 vertebrae and were compression tested to failure. For all models tested, the ultimate strength results showed that there was a reinforcing effect between the shell and the trabecular core which was not accounted for by the sum of the strength contributions of the shell and core when tested individually (Table 4). Although previous finite element studies on whole bone vertebrae have been limited to linear analysis and have not addressed ultimate strength properties, their results are consistent with the findings of this study. Bayraktar et al. reported that the cortical shell contributed 44% of the stiffness of the whole vertebra even though it occupied just 22.4% of the total bone volume and had an axial stiffness in isolation that was only 8% of the intact vertebral body (Bayraktar et al., 2003). In a subsequent FE study on thirteen human vertebrae, Eswaran et al. determined that a load fraction of 38% to 68% was carried by the cortical shell (Eswaran et al., 2007b, Eswaran et al., 2006) even though it only constituted 21% to 39% of the total volume of bone tissue.

The results of the 96 mm RP model tests revealed that the reinforcing effect between the shell and core increased from a low value of 2% of the isolated core strength for the un-thinned model to a value of 60% for the thinned model. This indicates that as the model size scale approaches whole bone dimensions, the reinforcing effect remains an important factor for lower volume fraction specimens. This increase in reinforcing effect with decreasing trabecular bone volume fraction was found to occur for all models tested.

The high value of reinforcing effect on the ultimate strength for the thinned models can be partially explained by the greater stiffness of the shelled model compared to the un-shelled model (Fig. 8). In the elastic region of the stress–strain curve, the load that is supported by the shelled model for a given applied strain is greater than the load supported by the un-shelled model, by a factor that is equal to the ratio of the respective modulus values. The mechanical

interaction between the shell and the core contributes to the increased stiffness of the shelled model via the core stiffening effect and the shell stiffening effect. The core stiffening effect is due to the higher stresses that occur in the trabecular core transition region for the shelled models compared to the un-shelled models. For the un-shelled models, the average annulus stresses drop off across this same transition region due to the side-artifact effect (Bevill et al., 2007, Un et al., 2006), i.e. the disconnected trabeculae at the outer surface of the core are unloaded. This reinforcing effect across the transition region is greater for the thinned model (BV/TV =0.22) compared to the un-thinned model (BV/TV =0.45). This due to the larger radial thickness of the transition region for the thinned model (1.09 mm) compared to the un-thinned model (0.66 mm) and also the fact that the stress differential across the transition region is greater for the lower volume fraction case.

The contribution of the shell stiffening effect to the overall stiffness of the shell–core structure was found to be greater than the contribution of the core stiffening effect, for all models tested (Table 5). In effect, the trabecular core provides reinforcement where it connects to the shell, thus inhibiting bending and buckling behaviour of the shell (Fig. 4). The combined shell stiffening effect and core stiffening effect provided a major contribution to the overall stiffness of the shell–core structure, ranging from 16.7% of the overall stiffness for un-thinned Model 4% to 38.2% for the thinned 96 mm model (calculated from Table 5).

Limitations of this study include the fact that an idealised, cylindrical shell–core architecture was used instead of a whole bone geometry. This was due to restrictions in the size of RP model that could be manufactured on the laser sinterstation. However, it is reasonable to infer that the shell–core interactions which occur for such an idealised geometry will also occur in a whole bone geometry. The reduced size scale of the models tested in this study compared to whole bone specimens is another limitation which results in a reduction of the trabecular load paths available to carry the applied loads. As the size scale increases, it is expected that the relative contribution of the core stiffening effect will decrease because the size of the trabecular core transition region relative to the overall core size is reduced. However, it is also expected that the contribution of the shell stiffening effect will increase because there is a greater propensity for buckling and bending effects to occur in larger diameter thin shells. Therefore, larger diameter shells will have a lower effective modulus and strength than smaller diameter shells, so that the potential reinforcing effect of the trabecular core on the shell is greater. Our results showed that as the size scale increased from 48 mm diameter to 96 mm diameter models, the reinforcing effect between the shell and the core remained an important contributor to the overall load bearing for the lower density, thinned model. Another limitation was the fact that uniform thinning of trabeculae was used to simulate bone loss. Age-related osteoporosis is more appropriately modelled by including a consideration of adaptive remodelling based on strain levels in the trabecular network under normal loading conditions. However, it is considered that the deterioration of mechanical properties due to uniform trabecular thinning in this study is sufficient to demonstrate the mechanisms by which the reinforcing effect between the shell and the trabecular core becomes more important as bone loss in the trabecular core increases. Finally, the stiffness analysis in this study, which was used to decouple the reinforcing effect into the contributions of the core stiffening effect and the shell stiffening effect, is based on the assumption that bone strength is directly correlated to bone stiffness. Although this assumption is supported by the results of previous studies (Fyhrie and Vashishth, 2000, Keaveny et al., 1994), there is scope in future work to extend the linear FE analysis that was used in this study to a more representative nonlinear failure analysis.

It should also be noted that the volume fraction of the ovine trabecular bone models used in this study is high ($BV/TV = 0.17-0.45$) compared to elderly trabecular bone from the human spine ($BV/TV = 0.04-0.12$) (Mosekilde, 2000). Our RP model test results showed that the ultimate strength reinforcing effect increased as the bone volume fraction decreased. This indicates that for lower volume fraction human bone, the reinforcing effect may be greater than that obtained for the relatively dense bone used in this study.

In conclusion, the results of the RP model tests and FE analyses indicate that the mechanical interaction between the trabecular core and the shell results in a reinforcing effect on the ultimate strength and stiffness of the overall structure which cannot be accounted for by the individual contributions of the shell and trabecular core in isolation. The relative importance of this reinforcing effect to the ultimate strength increases as the bone volume fraction of the trabecular core decreases. In the linear elastic region of the stress-strain curve, the reinforcing effect on the overall stiffness can be decoupled into the core stiffening effect and the shell stiffening effect. The shell stiffening effect has been found to be the more dominant contributor to the overall stiffness of the shell-core structure. From a clinical perspective, the results of this study imply that the maintenance of connectivity between the trabecular core and the cortical shell is desirable for preserving the reinforcing interaction which occurs between the shell and core. This is particularly the case for osteoporotic bone, since the reinforcing interaction becomes relatively more important to the shell-core ultimate strength as the trabecular core bone volume fraction decreases.

Acknowledgements

This work is part of the Bone for Life project, funded by the Programme for Research in Third Level Institutions (PRTL), administered by the Higher Education Authority in Ireland. The authors wish to acknowledge the SFI/HEA Irish Centre for High-End Computing (ICHEC) for the provision of computational facilities and support.

References

- Andresen, R., Werner, H.J., Schober, H.-C., 1998. Contribution of the cortical shell of vertebrae to mechanical behaviour of the lumbar vertebrae with implications for predicting fracture risk. *The British Journal of Radiology* 71, 759-765.
- Arthur Moore, T.L., Gibson, L.J., 2002. Microdamage accumulation in bovine trabecular bone in uniaxial compression. *Journal of Biomechanical Engineering* 124, 63-71.
- Bayraktar, H.H., Buckley, J.M., Adams, M.F., Gupta, A., Hoffmann, P.F., Lee, D.C., Papadopoulos, P., Keaveny, T.M., 2003. Cortical shell thickness and its contribution to vertebral body stiffness. In: 2003 Summer Bioengineering Conference Florida.
- Bayraktar, H.H., Keaveny, T.M., 2004. Mechanisms of uniformity of yield strains for trabecular bone. *Journal of Biomechanics* 37, 1671-1678.
- Bevill, G., Easley, S.K., Keaveny, T.M., 2007. Side-artifact errors in yield strength and elastic modulus for human trabecular bone and their dependence on bone volume fraction and anatomic site. *Journal of Biomechanics* 40, 3381-3388.

Caulfield, B., Mc Hugh, P., Lohfeld, S., 2007. Dependence of mechanical properties of polyamide components on build parameters in the SLS process. *Journal of Materials Processing Technology* 182, 477-488.

Ding, M., Odgaard, A., Linde, F., Hvid, I., 2002. Age-related variations in the microstructure of human tibial cancellous bone. *Journal of Orthopaedic Research* 20, 615-621.

Dobson, C.A., Sias, G., Phillips, R., Fagan, M.J., Langton, C.M., 2006. Three dimensional stereolithography models of cancellous bone structures from CT data: Testing and validation of finite element results. *Proceedings of the Institution of Mechanical Engineers Part H. Journal of Engineering in Medicine* 220, 481-484.

Eswaran, S.K., Allen, M.R., Burr, D.B., Keaveny, T.M., 2007a. A computational assessment of the independent contribution of changes in canine trabecular bone volume fraction and microarchitecture to increased bone strength with suppression of bone turnover. *Journal of Biomechanics* 40, 3424-3431.

Eswaran, S.K., Bayraktar, H.H., Adams, M.F., Gupta, A., Hoffmann, P.F., Lee, D.C., Papadopoulos, P., Keaveny, T.M., 2007b. The micro-mechanics of cortical shell removal in the human vertebral body. *Computer Methods in Applied Mechanics and Engineering* 196, 3025-3032.

Eswaran, S.K., Gupta, A., Adams, M.F., Keaveny, T.M., 2006. Cortical and trabecular load sharing in the human vertebral body. *Journal of Bone and Mineral Research* 21, 307-314.

Follet, H., Peyrin, F., Vidal-Salle, E., Bonnassie, A., Rumelhart, C., Meunier, P.J., 2007. Intrinsic mechanical properties of trabecular calcaneus determined by finite-element models using 3d synchrotron microtomography. *Journal of Biomechanics* 40, 2174-2183.

Fyhrie, D.P., Vashishth, D., 2000. Bone stiffness predicts strength similarly for human vertebral cancellous bone in compression and for cortical bone in tension. *Bone* 26, 169-173.

Goldstein, S.A., 1987. The mechanical properties of trabecular bone: Dependence on anatomic location and function. *Journal of Biomechanics* 20, 1055-1061.

Goulet, R.W., Goldstein, S.A., Ciarelli, M.J., Kuhn, J.L., Brown, M.B., Feldkamp, L.A., 1994. The relationship between the structural and orthogonal compressive properties of trabecular bone. *Journal of Biomechanics* 27, 375-377.

Guo, X.E., Kim, C.H., 2002. Mechanical consequence of trabecular bone loss and its treatment: A three-dimensional model simulation. *Bone* 30, 404-411.

Harrison, N., Mc Donnell, P., O'Mahoney, D., Kennedy, O., O'Brien, F.J., Mc Hugh, P., 2008. Heterogeneous linear elastic trabecular bone modelling using micro-CT attenuation data and experimentally measured heterogeneous tissue properties. *Journal of Biomechanics* 41, 2589-2596.

Homminga, J., McCreadie, B.R., Ciarelli, T.E., Weinans, H., Goldstein, S.A., Huiskes, R., 2002. Cancellous bone mechanical properties from normals and patients with hip fractures differ on the structure level not on the bone hard tissue level. *Bone* 30, 759-764.

Homminga, J., McCreadie, B.R., Weinans, H., Huiskes, R., 2003. The dependence of the elastic properties of osteoporotic cancellous bone on volume fraction and fabric. *Journal of Biomechanics* 36, 1461-1467.

Homminga, J., Weinans, H., Gowin, W., Felsenberg, D., Huiskes, R., 2001. Osteoporosis changes the amount of vertebral trabecular bone at risk of fracture but not the vertebral load distribution. *Spine* 26, 1555-1561.

Hou, F.J., Lang, S.M., Hoshaw, S.J., Reimann, D.A., Fyhrie, D.P., 1998. Human vertebral body apparent and hard tissue stiffness. *Journal of Biomechanics* 31, 1009-1015.

Hulme, P.A., Boyd, S.K., Ferguson, S.J., 2007. Regional variation in vertebral bone morphology and its contribution to vertebral fracture strength. *Bone* 41, 946-957.

Ito, M., Nishida, A., Koga, A., Ikeda, S., Shiraishi, A., Uetani, M., Hayashi, K., Nakamura, T., 2002. Contribution of trabecular and cortical components to the mechanical properties of bone and their regulating parameters. *Bone* 31, 351-358.

Keaveny, T.M., 1993. Trabecular bone modulus and strength can depend on specimen geometry. *Journal of Biomechanics* 26, 991-1000.

Keaveny, T.M., 1997. Systematic and random errors in compression testing of trabecular bone. *Journal of Orthopaedic Research* 15, 101-110.

Keaveny, T.M., Wachtel, E.F., Ford, C.M., Hayes, W.C., 1994. Differences between the tensile and compressive strengths of bovine tibial trabecular bone depend on modulus. *Journal of Biomechanics* 27, 1137-1146.

Kopperdahl, D.L., Keaveny, T.M., 1998. Yield strain behavior of trabecular bone. *Journal of Biomechanics* 31, 601-608.

Liebschner, M.A.K., 2004. Biomechanical considerations of animal models used in tissue engineering of bone. *Biomaterials* 25, 1697-1714.

Liebschner, M.A.K., Muller, R., Wimalawansa, S.J., Rajapakse, C.S., Gunaratne, G.H., 2005. Testing two predictions for fracture load using computer models of trabecular bone. *Biophysical Journal* 89, 759-767.

Linde, F., 1989. The effect of constraint on the mechanical behaviour of trabecular bone specimens. *Journal of Biomechanics* 22, 485-490.

Lohfeld, S., Barron, V., McHugh, P.E., 2005. Biomodels of bone: A review. *Annals of Biomedical Engineering* 33, 1295-1311.

Morgan, E.F., Bayraktar, H.H., Keaveny, T.M., 2003. Trabecular bone modulus-density relationships depend on anatomic site. *Journal of Biomechanics* 36, 897-904.

Mosekilde, L., 1990. Consequences of the remodelling process for vertebral trabecular bone structure: A scanning electron microscopy study (uncoupling of unloaded structures). *Bone and Mineral* 10, 13-35.

- Mosekilde, L., 2000. Age-related changes in bone mass structure and strength . Effects of loading. *Zeitschrift fur Rheumatologie* 59, I1-I9.
- Muller, R., Ruegsegger, P., 1995. Three-dimensional finite element modelling of non-invasively assessed trabecular bone structures. *Medical Engineering & Physics* 17, 126-133.
- Muller, R., Ruegsegger, P., 1996. Analysis of mechanical properties of cancellous bone under conditions of simulated bone atrophy. *Journal of Biomechanics* 29, 1053-1060.
- Nagaraja, S., Couse, T.L., Guldborg, R.E., 2005. Trabecular bone microdamage and microstructural stresses under uniaxial compression. *Journal of Biomechanics* 38, 707-716.
- Nazarian, A., Stauber, M., Zurakowski, D., Snyder, B.D., Muller, R., 2006. The interaction of microstructure and volume fraction in predicting failure in cancellous bone. *Bone* 39, 1196-1202.
- Newton, B.I., Cooper, R.C., Gilbert, J.A., Johnson, R.B., Zardiackas, L.D., 2004. The ovariectomized sheep as a model for human bone loss. *Journal of Comparative Pathology* 130, 323-326.
- Niebur, G.L., Feldstein, M.J., Yuen, J.C., Chen, T.J., Keaveny, T.M., 2000. High-resolution finite element models with tissue strength asymmetry accurately predict failure of trabecular bone. *Journal of Biomechanics* 33, 1575-1583.
- Ohman, C., Baleani, M., Perilli, E., Dall'Ara, E., Tassani, S., Baruffaldi, F., Viceconti, M., 2007. Mechanical testing of cancellous bone from the femoral head: Experimental errors due to off-axis measurements. *Journal of Biomechanics* 40, 2426-2433.
- Perilli, E., Baleani, M., Ohman, C., Fognani, R., Baruffaldi, F., Viceconti, M., 2008. Dependence of mechanical compressive strength on local variations in microarchitecture in cancellous bone of proximal human femur. *Journal of Biomechanics* 41, 438-446.
- Pouilles, J.M., Collard, P., Tremollieres, F., Frayssinet, P., Railhac, J.J., Cahuzac, J.P., Autefage, A., Ribot, C., 2000. Accuracy and precision of in vivo bone mineral measurements in sheep using dual-energy x-ray absorptiometry. *Calcified Tissue International* 66, 70-73.
- Silva, M.J., Gibson, L.J., 1997. Modeling the mechanical behavior of vertebral trabecular bone: Effects of age-related changes in microstructure. *Bone* 21, 191-199.
- Sran, M.M., Boyd, S.K., Cooper, D.M.L., Khan, K.M., Zernicke, R.F., Oxland, T.R., 2007. Regional trabecular morphology assessed by micro-ct is correlated with failure of aged thoracic vertebrae under a posteroanterior load and may determine the site of fracture. *Bone* 40, 751-757.
- Su, R., Campbell, G.M., Boyd, S.K., 2007. Establishment of an architecture-specific experimental validation approach for finite element modeling of bone by rapid prototyping and high resolution computed tomography. *Medical Engineering & Physics* 29, 480-490.
- Tanck, E., Ruimerman, R., Huiskes, R., 2006. Trabecular architecture can remain intact for both disuse and overload enhanced resorption characteristics. *Journal of Biomechanics* 39, 2631-2637.

- Thomas, T., Vico, L., Skerry, T.M., Caulin, F., Lanyon, L.E., Alexandre, C., Lafage, M.H., 1996. Architectural modifications and cellular response during disuse-related bone loss in calcaneus of the sheep. *Journal of Applied Physiology* 80, 198-202.
- Thomsen, J.S., Ebbesen, E.N., Mosekilde, L., 2002a. Age-related differences between thinning of horizontal and vertical trabeculae in human lumbar bone as assessed by a new computerized method. *Bone* 31, 136-142.
- Thomsen, J.S., Ebbesen, E.N., Mosekilde, L., 2002b. Predicting human vertebral bone strength by vertebral static histomorphometry. *Bone* 30, 502-508.
- Umeno, T., Takahashi, K., Hara, T., Tokunaga, K., Endo, N., 2006. Estimation of mechanical properties of trabecular bone using rapid prototyping technology. *Journal of Biomechanics* 39, S465.
- Un, K., Bevil, G., Keaveny, T.M., 2006. The effects of side- artifacts on the elastic modulus of trabecular bone. *Journal of Biomechanics* 39, 1955-1963.
- van der Linden, J.C., Verhaar, J.A., Weinans, H., 2002. A three-dimensional simulation of age-related remodeling in trabecular bone. *Journal of Bone and Mineral Research* 17, 688-696.
- Verhulp, E., van Rietbergen, B., Müller, R., Huiskes, R., 2008. Indirect determination of trabecular bone effective tissue failure properties using micro-finite element simulations. *Journal of Biomechanics* 41, 1479-1485.
- Wang, X., Niebur, G.L., 2006. Microdamage propagation in trabecular bone due to changes in loading mode. *Journal of Biomechanics* 39, 781-790.
- Yeh, O.C., Keaveny, T.M., 2001. Relative roles of microdamage and microfracture in the mechanical behavior of trabecular bone. *Journal of Orthopaedic Research* 19, 1001-1007.
- Yeni, Y.N., Fyhrie, D.P., 2001. Finite element calculated uniaxial apparent stiffness is a consistent predictor of uniaxial apparent strength in human vertebral cancellous bone tested with different boundary conditions. *Journal of Biomechanics* 34, 1649-1654.
- Zysset, P., Marsan, A., Chu, T.-M., Guldborg, R.E., Halloran, J.W., Hollister, S.J., 1997. Rapid-prototyping of trabecular bone for mechanical testing. In: *Proceedings of the 1997 Bioengineering Conference*, vol. 35. ASME, p. 387.

Tables

Table 1. Results of ultimate strength tests on real bone tissue specimens and PA-12 material. Real bone tissue specimens have been extracted from cortical shells of vertebrae

Parameter	Value	
	Real bone tissue (cortical shell specimen) N = 20 Mean \pm standard deviation	PA-12 N = 7 Mean \pm standard deviation
Specimen length (mm)	5.27 \pm 0.53	5.22 \pm 0.01
Specimen width (mm)	4.95 \pm 1.12	4.46 \pm 0.01
Specimen thickness (mm)	1.16 \pm 0.23	1.11 \pm 0.01
Ultimate stress (MPa)	104.30 \pm 30.94	41.84 \pm 3.25

Table 2. Ultimate stress results for real bone specimens and corresponding RP models. Real bone specimens are trabecular cores that have been extracted from vertebrae.

Specimen number	Ultimate strength (MPa)		
	RP model with correction factor	Real bone (trabecular core)	% Difference
1	23.23	25.16	-7.65
2 ^a	***	***	***
3	26.64	27.76	-4.01
4	23.68	25.34	-6.55
5 ^a	***	***	***
6	27.71	29.46	-5.91
7	18.23	23.75	-23.26
8 ^b	***	19.47	***
9	19.97	24.92	-19.88
10	22.91	27.02	-15.21
11 ^c	***	16.53	***
12	24.53	24.78	-1.00
13	23.78	26.66	-10.81
14	27.07	30.80	-12.13
15 ^{a, d}	***	***	***
16 ^d	***	32.49	***
17	28.16	31.54	-10.71
18	26.15	29.78	-12.22
19 ^{d, e}	***	53.79	***
20	17.65	20.10	-12.18

^a Specimen 2, 5, 15: real bone specimen results considered outliers due to incorrect mounting or damage to bone tissue during machining.

^b Specimen 8: RP model included un-removed debris from real bone specimen.

^c RP model 11 did not include location of real bone which failed.

^d RP models 15, 16 and 19: 25kN limit reached on test machine.

^e Specimen 19 incorporated a portion of solid cortical bone.

Table 3. Description of failure mechanisms for RP models and real bone specimens.

Specimen no.	Initial failure location		Failure description	
	RP model	Real bone	RP model	Real bone
1	Vertical struts and plates at bottom end of model	Same as for RP model	Buckling of vertical struts and plates	Buckling and shear of vertical struts and plates. Failure more brittle than RP model.
3	Vertical struts at top end of model	Same as for RP model	Buckling of vertical struts	Bending and shear of vertical struts
4	Central plate and struts	Same as for RP model	Shear of plate and strut. Buckling of vertical strut.	Same as for RP model
6	Top end of model	Bottom end of specimen	Bending of vertical struts	Shear of vertical struts
7	Plates in centre of model	Same as for RP model	Shear of plates	Shear of plates
9	Central plate at top end of model. Also vertical struts in centre of model	Same plate as for RP model. Also failure in end-cap	Shear of plate. Buckling of vertical struts.	Shear of plate. Failure in end-cap.
12	Vertical struts above centre of specimen	Same as for RP model	Ductile buckling of vertical struts	Failure of same struts as RP but failure mode more brittle.
13	Vertical struts on either side of vertebral vein	Same vertical struts below vertebral vein as RP model	Buckling of vertical struts	Bending of vertical struts
14	Vertebral vein	End-cap at bottom end of specimen	Buckling of plate at vertebral vein	Failure in end-cap
16	Top end of model near end plate	Same as for RP model	Bending of vertical struts	Bending and shear of vertical struts
18	Vertical struts and plates, below centre of model	Same as for RP model	Bending of vertical struts	Bending of vertical struts
20	Plate in centre of model	Vertical struts at top end of specimen	Buckling of plate and vertical strut	Buckling of vertical struts

1. It was not possible to directly compare 8 of the specimens with the RP replicas due to testing problems such as machine load limits being reached and video recording errors.
2. RP models 4, 12 have detailed similarities in failure mechanisms compared to real bone.
3. RP models 1, 3, 7, 9, 13, 16 and 18 fail in the same location and have similarities in failure mechanisms compared to real bone.
4. RP models 6, 14 and 20 fail in a different manner to real bone.

Table 4. Modulus results and strength reinforcing effect from RP model tests. The reinforcing load is calculated from the failure loads obtained from tests on the shell–core structure, the core without a shell and the shell on its own Eq. (3).

Specimen no.	BV/TV (core)	Shell–core modulus (MPa)	Core modulus (MPa)	% Reinforcing effect/trabecular core strength	% Reinforcing effect/shell–core strength
				$\% F_R/F_C$	$\% F_R/F_{SC}$
4 un-thinned	0.32	368	267	24	16
4 level 1 bone loss	0.25	305	178	48	25
4 level 2 bone loss	0.18	178	64	79	26
6 un-thinned	0.36	381	243	22	15
6 level 1 bone loss	0.28	343	229	35	21
6 level 2 bone loss	0.20	216	76	141	38
20 un-thinned	0.26	305	203	22	14
20 level 1 bone loss	0.17	241	102	90	33
96 mm un-thinned	0.45	390	330	2	2
96 mm thinned	0.22	101	37	60	31

The level 2 bone loss case for Model 20 resulted in a trabecular core that was too weak to be representative of real bone. Therefore, the results for this model are not presented.

Table 5. Modulus results — contribution of core reinforcing effect and shell reinforcing effect to overall modulus.

Model	E_{SC} Shell/core structure (MPa)	E_C Trabecular core (MPa)	E_S Shell in isolation (MPa)	$\nu_C E_{RC}$ Core reinforcing effect (MPa)	$\nu_S E_{RS}$ Shell reinforcing effect (MPa)	$\% \frac{\nu_C E_{RC}}{E_C}$
96 mm un- thinned	390	330	450	5.4	47.3	1.63
96 mm thinned	101	37	450	3.9	34.7	10.44
4 un- thinned	368	267	878	25.0	36.6	9.36
4 level 1 bone loss	305	178	878	26.4	55.7	14.83
6 un- thinned	381	243	878	17.5	80.2	7.20
6 level 1 bone loss	343	229	878	17.6	55.3	7.67
20 un- thinned	305	203	878	12.7	46.9	6.27
20 level 1 bone loss	241	102	878	8.5	82.1	8.37

The modulus values for the shell in isolation are the average results of 5 test repetitions for the 48 mm and 96 mm diameter shells.

Figures

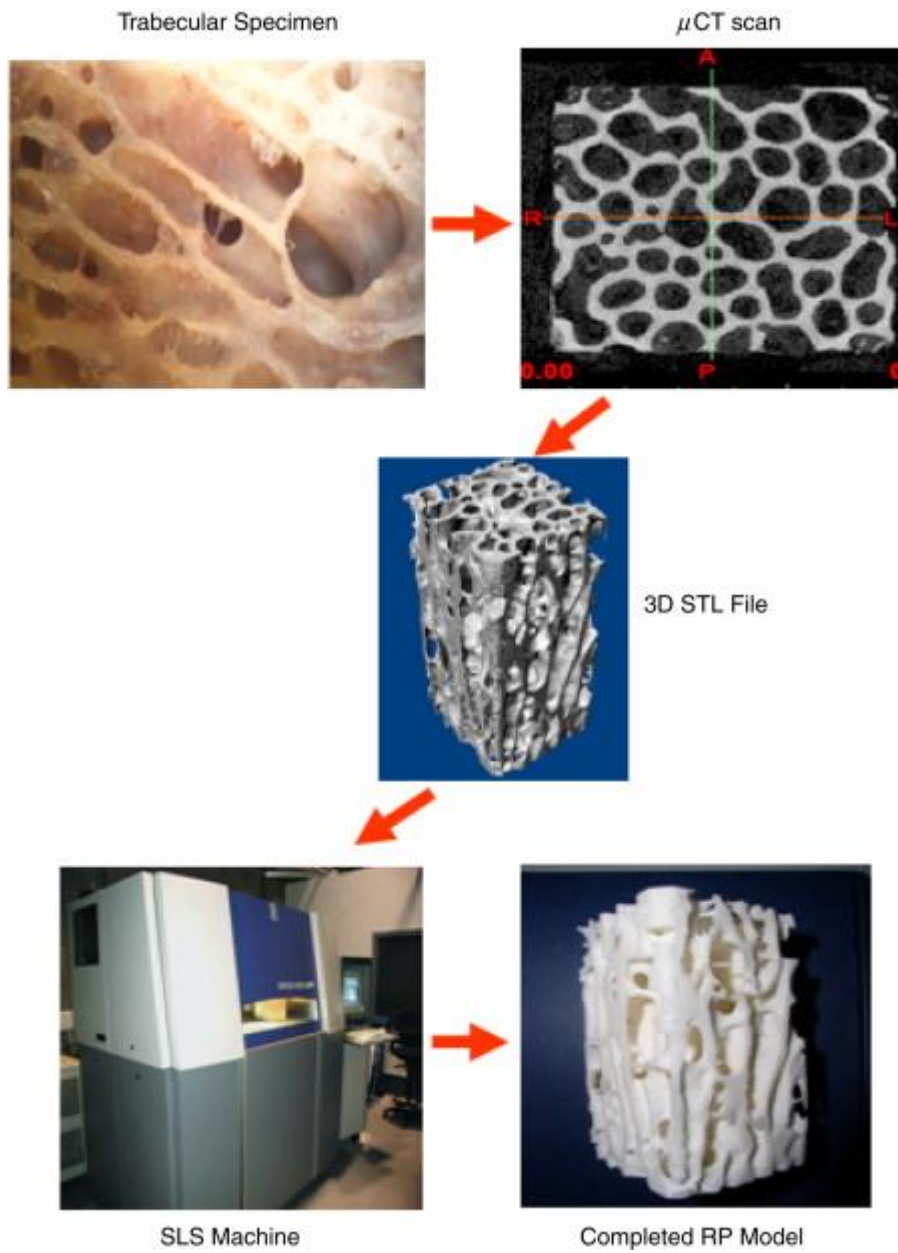


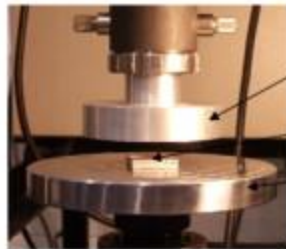
Fig. 1. Process for manufacturing RP model of trabecular bone.



1. Section of vertebral shell is extracted from same vertebrae that were originally used for testing trabecular cores.



2. Extracted section of vertebral shell. Attached trabecular bone has been removed using a scalpel and polishing disc, resulting in homogenous bone sample for subsequent compression testing.



Loading platen of test machine

Specimen mounted in holder

Support platen

3. Bone sample mounted in aluminium holder for compression test to failure in Instron testing machine.

Fig. 2. Extraction and testing of bone tissue specimen from vertebral shell. Picture 1 shows a vertebra from which a bone sample is extracted (marked by a black rectangle). Picture 2 shows extracted bone sample from the vertebral shell with attached trabeculae removed. Picture 3 shows the bone sample mounted in an aluminium holder and located between compression platens in an Instron testing machine, prior to compression testing.

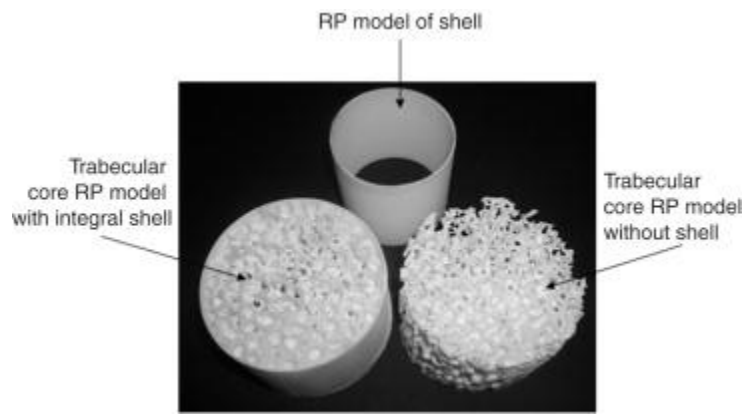
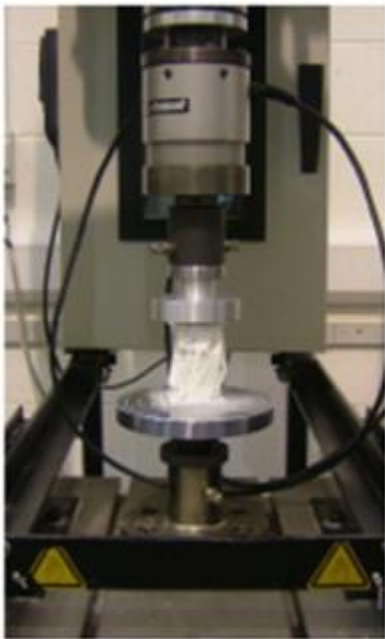
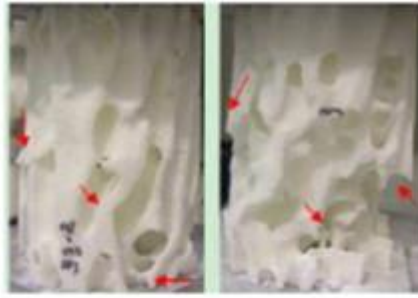


Fig. 3. RP Models for shell–core interaction study.



RP model in compression on Instron testing machine



Trabecular core models without shell



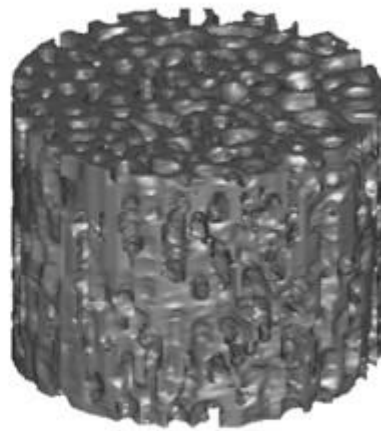
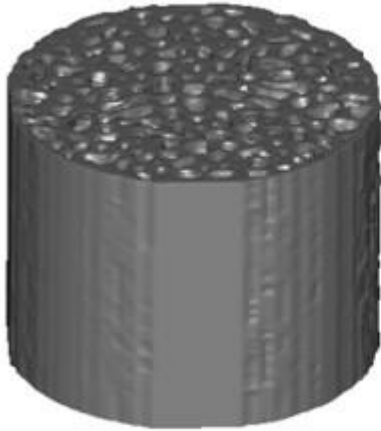
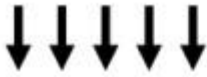
Trabecular core with integral shell



Shell without trabecular core

Fig. 4. Compression testing to failure of RP models (arrows indicate locations of permanent deformation).

0.5% strain applied to nodes on top surface



Nodes on bottom surface constrained
in all degrees of freedom

FE Model with Integral Shell

FE Model without Integral Shell

Fig. 5. Finite element models of 96 mm specimen.

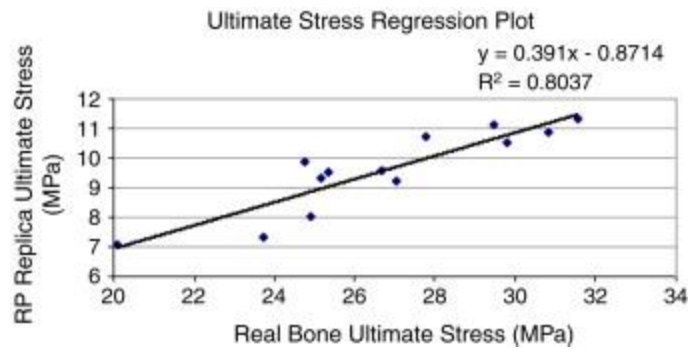


Fig. 6. Regression plot of RP replica ultimate stress versus real bone specimen ultimate stress.

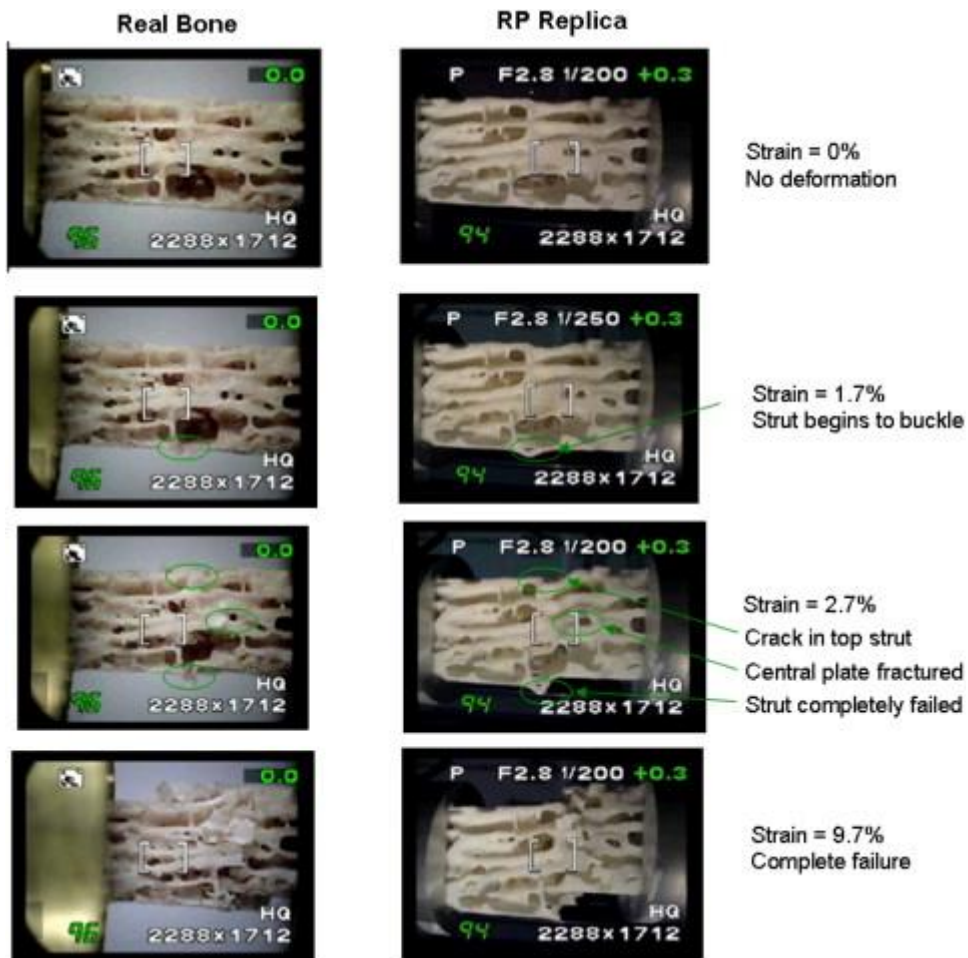


Fig. 7. Video still pictures which compare the deformation and failure mechanisms for real bone and RP replica (Specimen 4). The oval rings in the second and third rows indicate failure initiation.

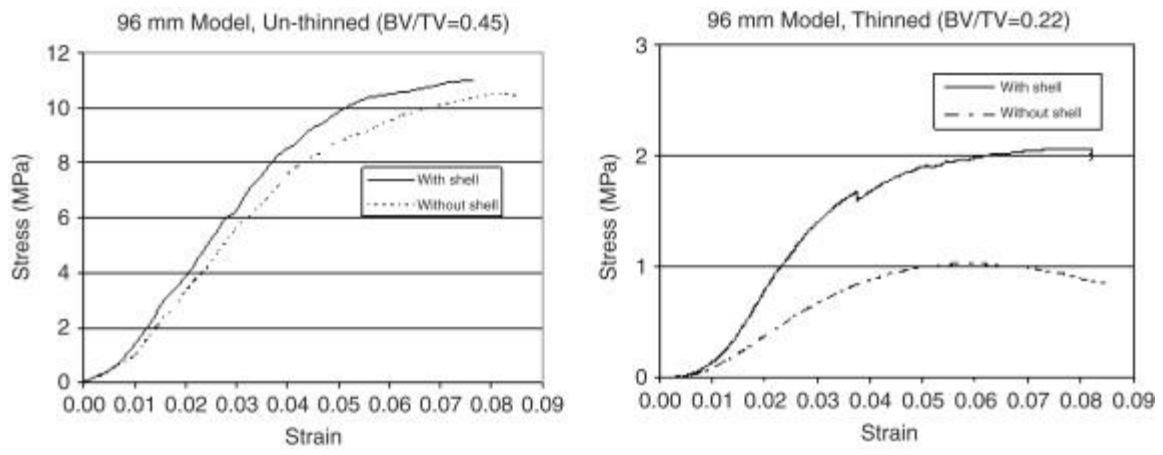
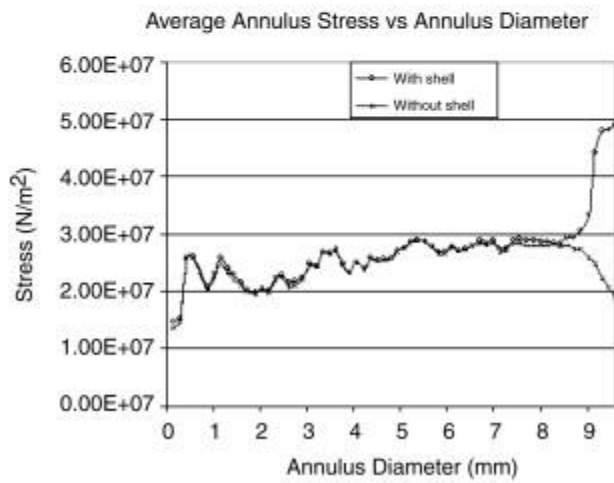
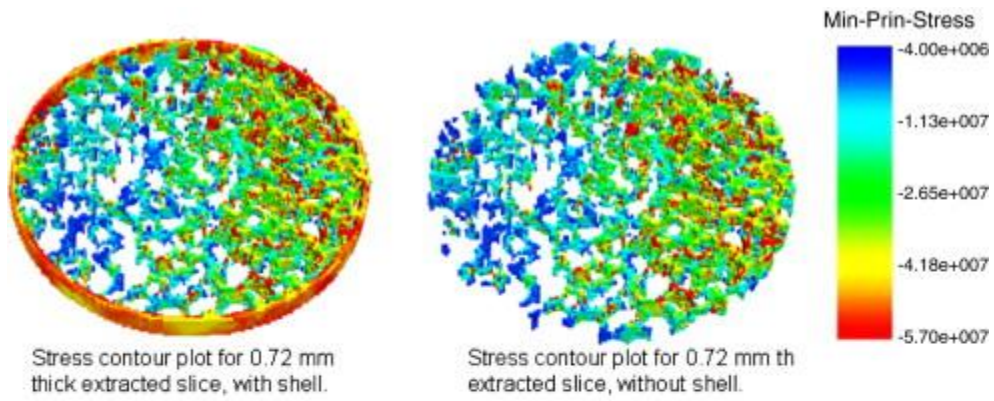


Fig. 8. Stress–strain curves for 96 mm diameter models.



Annulus diameter at 0 mm corresponds to centre of cylindrical specimen.
 Annulus diameter at 9.6 mm corresponds to outside surface of cylindrical specimen.

Fig. 9. Stress distribution results for 9.6 mm diameter, thinned model (BV/TV =0.22).